

**Magnetic structure and properties of the vanthoffite mineral  $\text{Na}_6\text{Mn}(\text{SO}_4)_4$** Ajana Dutta<sup>1</sup>, Diptikanta Swain<sup>2,\*</sup>, A. K. Bera<sup>3,4</sup>, Rajamani Raghunathan<sup>5</sup>, D. Samal<sup>4,6</sup>, S. M. Yusuf<sup>3,4</sup>, S. Ramasesha<sup>1</sup> and T. N. Guru Row<sup>1</sup><sup>1</sup>*Solid State and Structural Chemistry Unit, Indian Institute of Science, Bengaluru 560012, India*<sup>2</sup>*Institute of Chemical Technology–IndianOil Odisha Campus, Bhubaneswar 751013, India*<sup>3</sup>*Solid State Physics Division, Bhabha Atomic Research Centre, Mumbai 40085, India*<sup>4</sup>*Homi Bhabha National Institute, Anushaktinagar, Mumbai 400094, India*<sup>5</sup>*UGC-DAE Consortium for Scientific Research, Indore 452001, India*<sup>6</sup>*Institute of Physics, Bhubaneswar 751005, India* (Received 10 March 2022; revised 6 July 2022; accepted 26 August 2022; published 16 September 2022)

A detailed analysis of the magnetic properties of a vanthoffite-type mineral  $\text{Na}_6\text{Mn}(\text{SO}_4)_4$  based on dc magnetization, low-temperature neutron powder diffraction, and theoretical calculations is reported. The mineral crystallizes in a monoclinic system with space group  $P2_1/c$ , where  $\text{MnO}_6$  octahedra are linked via  $\text{SO}_4$  tetrahedra, forming a two-dimensional (2D) sheet structure in the  $bc$  plane of the crystal. This gives rise to superexchange interaction between two  $\text{Mn}^{2+}$  ions mediated by two nonmagnetic bridging anions ( $\text{Mn-O-O-Mn}$ ) and leads to an antiferromagnetic ordering below 3 K. The magnetic structure derived from neutron powder diffraction at 1.7 K depicts an antiferromagnetic spin arrangement in the  $bc$  plane. The magnetic properties are modeled by numerical calculations using an exact diagonalization technique, which fits the experimental results and also provides the antiferromagnetic ground state of  $\text{Na}_6\text{Mn}(\text{SO}_4)_4$ . Both experimental and theoretical calculation reveal a quasi-2D type of magnetic interaction in this polyanionic system, where the dominant antiferromagnetic interaction exists in the plane. The determined collinear antiferromagnetic ground state is consistent with the theoretical predictions for a  $J_1 - J_2$  Heisenberg triangular antiferromagnetic model.

DOI: [10.1103/PhysRevB.106.094419](https://doi.org/10.1103/PhysRevB.106.094419)**I. INTRODUCTION**

Over the last two decades, the design of polyanionic materials  $[(X\text{O}_4)_n]$  with  $X = \text{S, P, As, V, Si, Mo, or W}$  has attracted significant attention due to their adaptability towards various potential applications. For example, discovery and commercialization of  $\text{LiFePO}_4$  [1,2] has significantly contributed to the use of insertion materials in battery research [3–6]. In general, the coupling between magnetic and electrical properties in  $3d$ -metal-based polyanionic compounds invokes a magnetoelectric effect [7–18] which can be successfully utilized to design various multiferroic materials [19–21].  $\text{TbPO}_4$  is yet another such material which exhibits intrinsic bulk magnetoelectric effects [22,23]. In this context, the presence of polyanionic units in naturally occurring minerals offer a treasure trove of materials with associated tunable properties. Additionally, the presence of  $3d$  transition metals in the chemical composition of such minerals also offers the possibility of synthesizing solids with interesting magnetic behavior. Several electrode materials inspired by the naturally occurring minerals have been investigated, leading to the discovery of interesting magnetic properties in these materials [7,8,24–27]. A series of polyanionic phosphates  $\text{LiMPO}_4$  ( $M = \text{Mn, Co, Ni, or Fe}$ ) have been of special interest to evaluate the associated magnetic behavior in these minerals [15,28–32].

The origin of magnetic interactions in these transition-metal oxides, sulfates, phosphates, and arsenates are due to the overlap of the  $3d$  orbitals of the transition metal with the  $2p$  orbitals of the oxygen atom. In such superexchange interactions either two magnetic metal centers are bridged via a single electronegative anion, like oxygen ( $M\text{-O-M}$ ), or two metal centers interact via two oxygen atoms ( $M\text{-O-O-M}$ ), leading to a weaker magnetic interactions. A set of semiempirical rules referred to as Goodenough-Kanamori-Anderson rules, which these systems follow, are well described in the literature [33–38].

The magnetic structure of anhydrous  $\text{FeSO}_4$  and  $\text{NiSO}_4$  have antiferromagnetic sheets with ferromagnetic coupling between the sheets, whereas in the case of  $\text{CoSO}_4$ , only antiferromagnetic ordering exists within each sheet. On the other hand, the magnetic structure of  $\text{CrVO}_4$  has ferromagnetically ordered sheets that stack antiferromagnetically. However, in each case, magnetic coupling involves a long superexchange pathway between magnetic centers via nonmagnetic sulfate or vanadate tetrahedron [39].

In our ongoing research program which studies “minerals to functional materials,” we have studied temperature-induced phase transitions on a variety of materials with an emphasis on producing materials which display interesting physicochemical properties [40–45]. These include the variable-temperature structural analysis of compounds containing all transition metals. In this context we have synthesized a series of vanthoffite minerals in our laboratory which otherwise occur

\*Corresponding author: diptisscu@gmail.com

abundantly in nature as oceanic salt deposits [44–46]. The presence of Mn having five unpaired  $d$  electrons ( $3d^5$ ) in the structure of  $\text{Na}_6\text{Mn}(\text{SO}_4)_4$  opens up the possibility of designing a magnetic material with the desired properties. In our earlier work we have shown that the crystal structure of  $\text{Na}_6\text{Mn}(\text{SO}_4)_4$  is built from an alternating corner sharing of  $\text{SO}_4$  tetrahedra and transition-metal octahedra  $\text{MnO}_6$ , resulting in an infinite two-dimensional (2D) framework in the  $bc$  plane of the crystal [44]. Such specific connectivity suggests the possibility of a long magnetic exchange pathway between two  $\text{Mn}^{2+}$  centers via two oxygen atoms (Mn-O-O-Mn). Further, the magnetically active ion ( $\text{Mn}^{2+}$ ) connects four first nearest neighbors along the face diagonal and two second neighbors along the  $c$ -axis, forming a hexagonal 2D layered structure with triangular arrangement of Mn atoms in the  $bc$  plane, which repeats along the  $a$  axis of the crystal. This peculiar structural arrangement is unique among the polyanionic-type materials and is expected to give interesting magnetic properties via superexchange interaction among Mn atoms (Mn-O-O-Mn) with two different exchange strengths  $J_1$  and  $J_2$ . Furthermore, the triangular nature of the Mn sublattice could result in nontrivial magnetic ground states when there are competing exchange interactions, and hence investigating its magnetic properties would be of fundamental interest. Theoretically it is known that a 2D triangular lattice would result a collinear antiferromagnetic ground state when the ratio of in-plane exchange constants ( $J_2/J_1$ ) is less than 0.5 and a helical antiferromagnetic ground state for  $J_2/J_1$  beyond 0.5 [47]. These unique structural aspects of  $\text{Na}_6\text{Mn}(\text{SO}_4)_4$  motivated us to investigate the magnetic structure and properties of this material using variable-temperature neutron diffraction and dc magnetization measurements. Besides, we have also carried out numerical calculation using exact diagonalization techniques to shed light on the magnetic ground state and exchange interaction between manganese ions in the crystal. We found the ground state to be collinear from neutron diffraction with  $\mathbf{k} = (0,0,0)$  under the space group  $P2_1/c$ , which indicates that the material could be a linear magnetoelectric [7,8]. Our numerical calculation of susceptibility data also confirms the singlet spin ground state. Additionally, the ratio of in-plane exchange constants ( $J_2/J_1$ ) derived from theoretical calculations turns out to be 0.26, consistent with the antiferromagnetic ground state [47].

## II. EXPERIMENTAL METHOD

Single crystals of  $\text{Na}_6\text{Mn}(\text{SO}_4)_4$  were grown by slow evaporation at  $80^\circ\text{C}$  from an aqueous solution containing a 3:1 stoichiometric molar ratio of  $\text{Na}_2\text{SO}_4$  (Sigma-Aldrich, 99.99%) and  $\text{MnSO}_4 \cdot \text{H}_2\text{O}$  (Sigma-Aldrich, 99.99%), as described in the earlier publication [44]. Colorless block-shaped crystals were obtained after 15 days. The single-crystal x-ray diffraction (XRD) of the as-grown crystal was carried out on an Oxford Xcalibur (Mova) diffractometer equipped with an EOS CCD detector and a microfocus sealed tube using  $\text{Mo K}\alpha$  X radiation ( $\lambda = 0.71073 \text{ \AA}$ ; 50 kV and 0.8 mA), and the structural parameters agree with the earlier report [44]. Single crystals were crushed to form bulk polycrystalline powder for further characterization. Room-temperature powder XRD (PXRD) data was recorded on a PANalytical X'Pert PRO

diffractometer using a  $\text{Cu K}\alpha$  X radiation source in a  $2\theta$  range of  $8^\circ$ – $40^\circ$  with a step size of  $0.013^\circ$ . X'PERT HIGH SCORE PLUS (version 4.8) [48] was used to analyze the pattern, and profile fitting refinements were carried out using the room-temperature unit-cell parameters of  $\text{Na}_6\text{Mn}(\text{SO}_4)_4$  [44] in JANA2006 [49]. Profile parameters such as GU, GV, GW, LX, and LY were refined using Pseudo-Voigt function. Neutron diffraction patterns over a wide  $Q$  range ( $4\pi \sin \theta/\lambda = 0.3$ – $9.5 \text{ \AA}^{-1}$ , where  $2\theta$  and  $\lambda$  are the scattering angle and wavelength of the incident neutron beam, respectively) were recorded over 1.7–300 K by using the powder diffractometer PD-II ( $\lambda = 1.2443 \text{ \AA}$ ) at the Dhruva reactor, Trombay, India [50]. For the neutron diffraction measurements, the powder sample was filled in a vanadium can of diameter 6 mm. All the low-temperature measurements were performed by using a closed-cycle helium refrigerator. The neutron diffraction patterns were analyzed by a Rietveld refinement method using the FULLPROF suite program [51–55]. Temperature- and magnetic-field-dependent dc susceptibility measurements were probed with a commercial vibrating sample magnetometer (Cryogenic Co. Ltd., UK). The temperature-dependent magnetization curves [ $M$  vs  $T$ ] were recorded in the warming cycles over the temperature range of 2–300 K in both zero-field-cooled (ZFC) and field-cooled (FC) conditions. The isothermal magnetization curve was measured at 2 K in the increasing and decreasing field cycles up to 90 kOe.

## III. RESULTS AND DISCUSSION

$\text{Na}_6\text{Mn}(\text{SO}_4)_4$  belongs to a monoclinic system, space group  $P2_1/c$  with  $Z = 2$  as determined from single-crystal x-ray diffraction for the present work, and agrees well with the earlier report by our group [44]. Figure 1(a) shows the packing diagram viewed down the  $c$  axis extracted from x-ray diffraction, illustrating alternative corner-shared sulfate tetrahedra and manganese octahedra. The fractional coordinates of all atoms and the bond lengths and angles for  $\text{MnO}_6$  octahedra are given in Tables I and II. The asymmetric unit contains half the formula unit, where the Mn atom is in a special position (Wyckoff position  $2a$ , local site symmetry  $-1$ ), along with three sodium atoms and two sulfate units in general position (Wyckoff position  $4e$ , local site symmetry 1) (Table I). The Mn atom forms  $\text{MnO}_6$  octahedra with symmetrically related oxygen atoms and connected to  $\text{SO}_4$  tetrahedra in a “pinwheel pattern” [Fig. 1(b)] [56]. The  $\text{Mn}(\text{SO}_4)_6$  building blocks form an infinite two-dimensional framework along the  $bc$  plane [Fig. 1(c)]. This particular structural arrangement solely enables the  $M$ -O-O- $M$  exchange pathway between transition-metal ions [Fig. 1(d)], and arrangement of the Mn sublattice is shown in Fig. 1(e).

The Mn-O bond lengths in the  $\text{MnO}_6$  octahedra vary between 2.1597(12) and 2.1901(13)  $\text{\AA}$  (Table II), where the bond-length distortion parameters and bond-angle variance are calculated using formulas  $\Delta d = (\frac{1}{6}) \sum_n [\frac{d_n - d_{av}}{d_{av}}]^2$  and  $\sigma_{\text{oct}}^2 = \frac{1}{11} \sum_i [\alpha_i - 90]^2$  ( $d_n$  and  $d_{av}$  are the individual and average Mn-O bond length, and  $\alpha_i$  are the individual O-Mn-O bond angles) [57–59]. It is to be noted that  $\Delta d$  and  $\sigma_{\text{oct}}^2$  values for an ideal octahedron should be exactly zero. The bond-length distortion parameter obtained ( $\Delta d = 3.35 \times 10^{-5}$ ), though, indicates a quite symmetrical  $\text{MnO}_6$  octahedra,

TABLE I. Crystallographic details and fractional atomic coordinates for  $\text{Na}_6\text{Mn}(\text{SO}_4)_4$ .

Empirical formula = $\text{Na}_6\text{Mn}(\text{SO}_4)_4$ , formula weight (g/mol) = 577.12, space group = $P2_1/c$ , $a = 9.7131(13) \text{ \AA}$ , $b = 9.2926(11) \text{ \AA}$ , $c = 8.2609(12) \text{ \AA}$ , $\beta = 112.988(7)^\circ$ , $V = 686.42(16) \text{ \AA}^3$ , $R_{\text{obs}}[I > 2\sigma(I)] = 0.0183$ , $wR_{\text{obs}}[I > 2\sigma(I)] = 0.0541$							
Atom	Wyckoff position	Occupancy	x/a	y/b	z/c	$u_{\text{iso}}(\text{Å}^2)$	BVS
Mn1	2a	0.5	0.000000	0.000000	0.000000	0.01093(11)	1.927
Na1	4e	1	0.11489(9)	0.36352(8)	0.18562(11)	0.02590(19)	1.079
Na2	4e	1	0.31418(8)	-0.01160(7)	0.46824(9)	0.01645(17)	1.105
Na3	4e	1	0.43369(9)	-0.15142(8)	0.07766(10)	0.02486(19)	1.060
S1	4e	1	0.34511(4)	0.15332(4)	0.16518(5)	0.01101(12)	6.028
S2	4e	1	0.14234(4)	-0.30579(4)	0.21800(5)	0.01055(12)	6.060
O1	4e	1	0.20375(13)	0.10249(13)	0.17787(15)	0.0159(3)	2.038
O2	4e	1	0.33934(14)	0.31084(13)	0.15062(16)	0.0173(3)	2.134
O3	4e	1	0.36223(15)	0.08889(14)	0.01351(17)	0.0222(3)	2.043
O4	4e	1	0.46806(13)	0.11001(14)	0.32974(17)	0.0201(3)	2.110
O5	4e	1	0.02432(14)	-0.19349(13)	0.15358(17)	0.0176(3)	2.046
O6	4e	1	0.28843(14)	-0.23682(14)	0.30234(18)	0.0218(3)	1.979
O7	4e	1	0.13626(14)	-0.39575(13)	0.06987(16)	0.0196(3)	2.061
O8	4e	1	0.11064(16)	-0.39682(14)	0.34471(18)	0.0229(3)	1.983

the calculated bond-angle variance of 18.32 shows a distorted  $\text{MnO}_6$  octahedra. The bond valence sum for Mn atom is calculated to be around 1.927 using the Zachariasen formula  $V_i = \sum_j s_{ij} = \sum_j e^{\frac{d_0 - d_{ij}}{0.37}}$ , and it is in good agreement with the expected valance of +2 [60]. These are isolated  $\text{MnO}_6$  octahedra (pink) and are connected to  $\text{SO}_4$  tetrahedra (yellow) via their oxygen vertices (Fig. 1). Thus the structure presents an exchange pathway via two bridged oxygen atoms, viz., Mn-O-O-Mn magnetic interaction, where the Mn-O-O-Mn dihedral angle is about  $148^\circ$  [Fig. 1(d)]. A similar long exchange pathway ( $M$ -O-O- $M$ ) is found in  $\text{Li}_2M(\text{SO}_4)_2$ , ( $M = \text{Ni, Co, Fe, Mn}$ ), where magnetism in the materials is explained based on this interaction [7,8,24]. The single crystals grown are further crushed to form the powder sample, and the phase purity was checked using PXRD measurement. The PXRD profile refinement ( $R_p = 3.43$ ,  $R_{wp} = 4.50$ , and  $\chi^2 = 1.01$ ) at room temperature was carried out using the cell parameter and space group obtained from the single-crystal XRD, where the close similarity between the observed and the calculated patterns suggests the purity of the desired compound,  $\text{Na}_6\text{Mn}(\text{SO}_4)_4$  (Fig. 2).

### A. Magnetic measurements

The zero-field-cooled susceptibility curve of  $\text{Na}_6\text{Mn}(\text{SO}_4)_4$  measured under a magnetic field of 50 Oe [Fig. 3(a)] shows a peak revealing a transition to an antiferromagnetic (AFM) state below  $T_N \sim 3$  K. The AFM ordering is confirmed by our zero-field neutron diffraction study presented later. Figure 3(b) shows the

temperature-dependent susceptibility curve measured under 1000 Oe over the temperature range 2–300 K. The  $\chi$  vs  $T$  curve in Fig. 3(b), however, does not exhibit any distinct magnetic transition, in contrast to the observation made under a weak applied field of 50 Oe in Fig. 3(a). It is to be noted that the ZFC  $\chi T$  vs  $T$  plot under 1000 Oe [inset of Fig. 3(b)] yields a downturn below 20 K. This corroborates the existing antiferromagnetic interactions in  $\text{Na}_6\text{Mn}(\text{SO}_4)_4$ . We also notice that the  $\chi T$  value in the high-temperature (paramagnetic) region increases slightly with temperature, contrary to the constant value expected in the paramagnetic region. The reason for the same could be attributed to the additional contribution arising from the van Vleck paramagnetism ( $\chi_{VV}$ ), which is discussed in the theoretical section.

The inverse ZFC susceptibility plot under 1000 Oe is shown in Fig. 3(c). The linear fit to the inverse susceptibility curve yields the Curie-Weiss temperature  $\Theta_{CW} = -6.0$  K and the effective paramagnetic moment  $\mu_{\text{eff}} = 5.8 \mu_B/\text{f.u.}$  The observed value of the effective moment  $5.8 \mu_B/\text{f.u.}$  is in good agreement with the theoretically expected  $\mu_{\text{eff}}$  [where  $\mu_{\text{eff}}(s) = g\sqrt{s(s+1)}$ , with  $g = 2$ , Lande  $g$  factor] value of  $5.92 \mu_B/\text{Mn}^{2+}$ , considering only spin moment. This result confirms a +2 oxidation state of the magnetic Mn ion ( $s = 5/2$ ) in  $\text{Na}_6\text{Mn}(\text{SO}_4)_4$ . The isothermal field-dependent magnetization curve (Fig. 4) measured at 2 K shows a linear increase in the low-field regime and then tends to show a change in slope above 35 kOe and a saturation above 65 kOe. However, we do not observe any opening of the hysteresis loop (inset in Fig. 4) under field sweeping. The observation

TABLE II. Bond lengths and bond angles for  $\text{Na}_6\text{Mn}(\text{SO}_4)_4$ .

Bond	Length (Å)	Bond	Angle (°)	Bond	Angle (°)
Mn1-O5×2	2.1597(12)	O5-Mn1-O1×2	96.08(5)	O5-Mn1-O8×2	90.78(5)
Mn1-O1×2	2.1706(12)	O5-Mn1-O1×2	83.92(5)	O1-Mn1-O8×2	86.42(5)
Mn1-O8×2	2.1901(13)	O5-Mn1-O8×2	89.22(5)	O1-Mn1-O8×2	93.58(5)

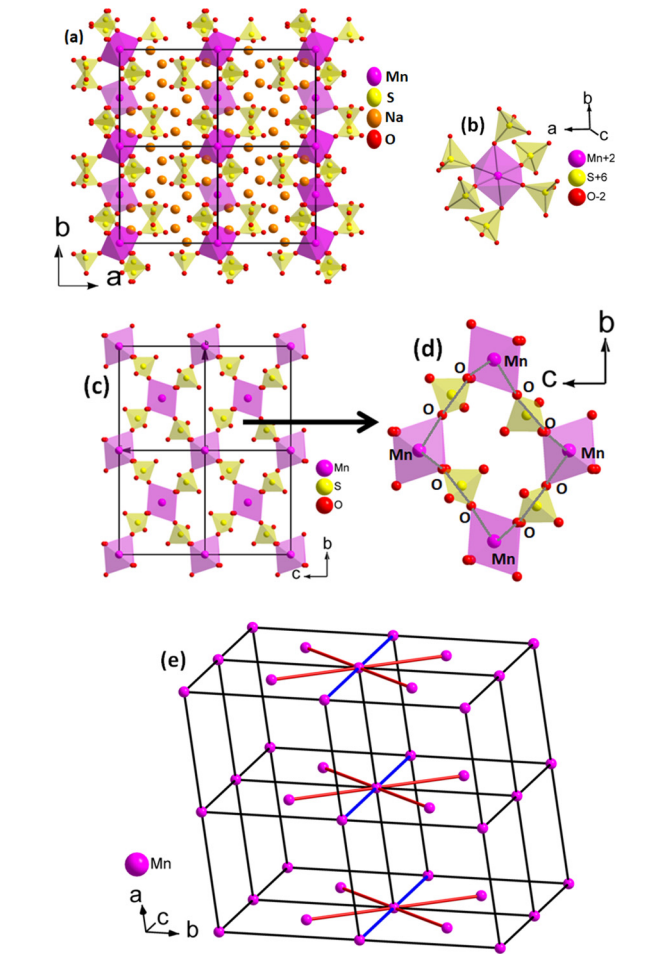


FIG. 1. (a) Packing diagram of  $\text{Na}_6\text{Mn}(\text{SO}_4)_4$  extracted from x-ray diffraction viewed down the  $c$  axis. (b) Highlighting the connectivity between  $\text{MnO}_6$  and  $\text{SO}_4$  tetrahedra. (c) Packing diagram viewed down the  $a$  axis, sodium atoms are removed for the clarity of the picture. (d)  $\text{Mn-O-O-Mn}$  interaction pathway through  $\text{MnO}_6$  octahedra and  $\text{SO}_4$  tetrahedra. (e) Arrangement of Mn sublattice in the structure showing the nearest neighbors (red bonds) and next-nearest neighbors (blue bonds).

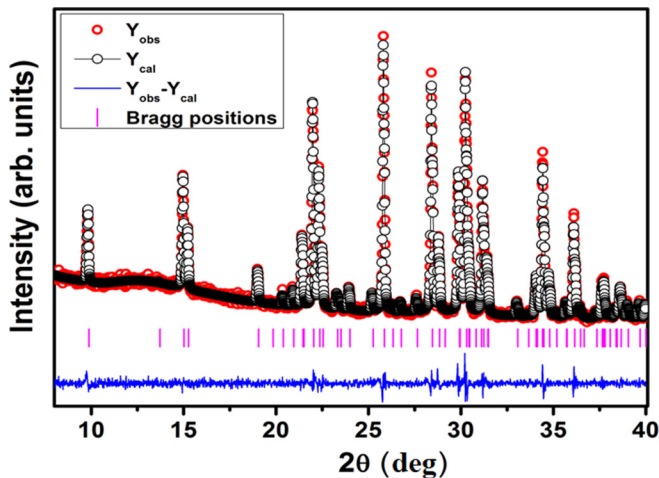


FIG. 2. PXRD Le Bail profile refinement of  $\text{Na}_6\text{Mn}(\text{SO}_4)_4$  at room temperature.

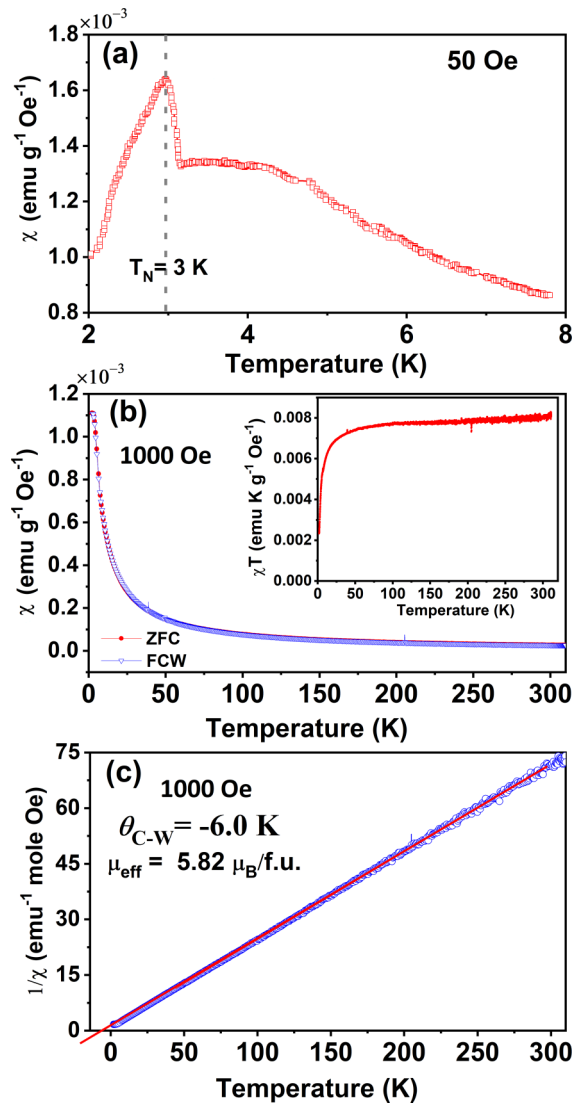


FIG. 3. (a) Low-temperature susceptibility curve measured under 50 Oe in ZFC mode. (b) The temperature-dependent susceptibility [ $\chi(T)$ ] curves measured under 1000 Oe in the ZFC and FCW modes. Inset shows  $\chi T$  vs  $T$  plot in the ZFC mode. (c) The inverse ZFC susceptibility as a function of temperature under 1000 Oe. The solid curve is a straight line fit to the measured data.

of negative Curie-Weiss temperature, downturn of  $\chi T$  vs  $T$ , linear magnetization behavior in the low-field region, and the absence of hysteresis altogether suggest an antiferromagnetic ground state of  $\text{Na}_6\text{Mn}(\text{SO}_4)_4$ .

## B. Neutron diffraction

In order to further investigate the magnetic ground state of the material, neutron diffraction data were collected on bulk powder sample over the temperature range 1.7–300 K. Preparation of a phase-pure compound in sufficient quantity to perform neutron diffraction is rather challenging. However, almost 5 g of single crystals were grown in different batches, and these crystals were crushed to form a polycrystalline powdered sample. The phase purity of a bulk amount of powdered sample was checked via laboratory PXRD. The Rietveld

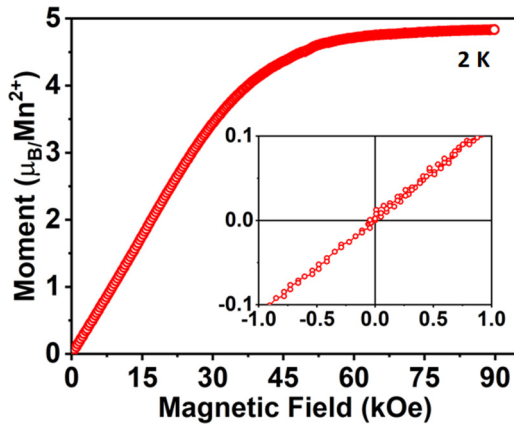


FIG. 4. The isothermal magnetization measured at 2 K after cooling the sample in zero field. Inset shows a zoomed view in the low-field region over  $\pm 1$  kOe and absence of hysteresis.

refined neutron diffraction patterns measured at 300 and 10 K are shown in Fig. 5. The crystal structure for  $\text{Na}_6\text{Mn}(\text{SO}_4)_4$  remains monoclinic with space group  $P2_1/c$  over the entire temperature range 1.7–300 K.

In order to probe the long-range antiferromagnetic interaction in  $\text{Na}_6\text{Mn}(\text{SO}_4)_4$ , neutron diffraction data were collected down to 1.7 K (Fig. 6). The appearance of additional magnetic Bragg peaks at  $2\theta \sim 7.6^\circ, 9.4^\circ$ , and  $11^\circ$  (marked with asterisks in Fig. 6) below 3 K confirms a long-range antiferromagnetic ordering of the material.

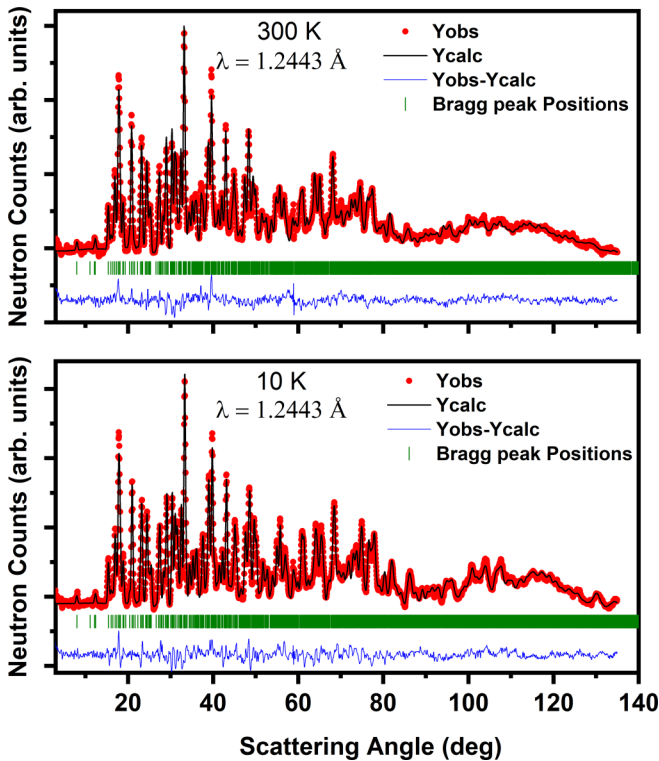


FIG. 5. Rietveld refinement of neutron diffraction patterns for  $\text{Na}_6\text{Mn}(\text{SO}_4)_4$  measured at (top) 300 K and (bottom) 10 K.

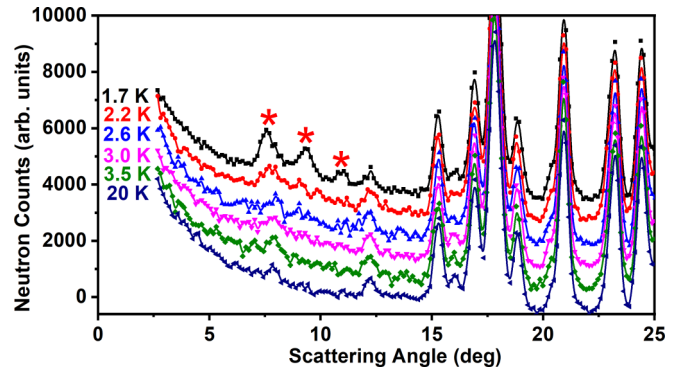


FIG. 6. Low-temperature neutron diffraction patterns down to 1.7 K.

All magnetic reflections observed for  $\text{Na}_6\text{Mn}(\text{SO}_4)_4$  could be indexed with a propagation vector  $\mathbf{k} = (0,0,0)$  with respect to the same monoclinic unit cell as the nuclear structure. The symmetry-allowed magnetic structure is determined by a representation analysis, as applied for various kinds of spin systems [61–64], using the program BASIREPS, available with the FULLPROF program suite [51]. The results of the symmetry analysis reveal that there are four irreducible representations (IRs). Among the four IRs, the IR(1) or  $\Gamma_1$  and IR(3) or  $\Gamma_3$  are nonzero for the magnetic site of the present compound. Therefore there are two possible symmetry-allowed magnetic structures for  $\text{Na}_6\text{Mn}(\text{SO}_4)_4$ . Both the IRs,  $\Gamma_1$  and  $\Gamma_3$ , are one dimensional.

The magnetic representation  $\Gamma_{\text{mag}}$  is composed as

$$\Gamma_{\text{mag}} = 3\Gamma_1 + 3\Gamma_3. \quad (1)$$

The basis vectors (the Fourier components of the magnetization) for these two IRs,  $\Gamma_1$  and  $\Gamma_3$  for the magnetic site, are given in Table III. The basis vectors are calculated using the projection operator technique implemented in the BASIREPS program [51,65]. Out of the  $\Gamma_1$  and  $\Gamma_3$ , the best refinement of the magnetic diffraction pattern is obtained for the IR  $\Gamma_1$ . The refinement with the  $\Gamma_1$  is shown in Fig. 7. A good agreement is observed between observed and calculated pattern.

The corresponding magnetic structure is shown in Fig. 8. The magnetic structure reveals antiferromagnetic chains of the

TABLE III. Basis vectors of the magnetic sites of Mn with the propagation vector  $\mathbf{k} = (0\ 0\ 0)$  for  $\text{Na}_6\text{Mn}(\text{SO}_4)_4$ . Only the real components of the basis vectors are presented. The two atoms of the nonprimitive basis are defined according to Mn-1 ( $x, y, z$ ):(0.5, 0, 0.5) and Mn-2 ( $-x, y + 1/2, -z + 1/2$ ):(-0.5, 0.5, 0).

IRs		Basis vectors	
		Site ( $2b$ )	
		Mn-1	Mn-2
$\Gamma_1$	$\Psi_1$	100	-100
	$\Psi_2$	010	010
	$\Psi_3$	001	00-1
$\Gamma_2$	$\Psi_1$	100	100
	$\Psi_2$	010	0-10
	$\Psi_3$	001	001

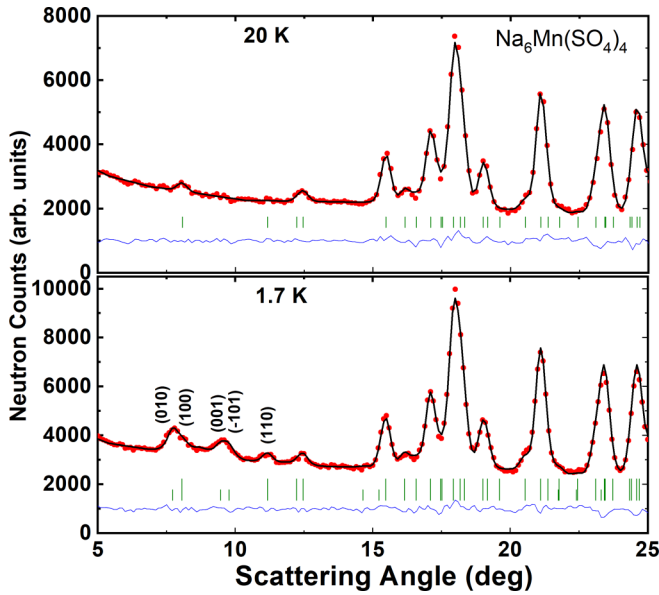


FIG. 7. Experimentally observed (circles) and calculated (solid lines through the data points) neutron diffraction patterns for  $\text{Na}_6\text{Mn}(\text{SO}_4)_4$  at (top) 20 K (paramagnetic state) and (bottom) 1.7 K (magnetically ordered state), respectively. The solid lines at the bottom of each panel represent the difference between observed and calculated patterns. The vertical bars indicate the positions of allowed nuclear and magnetic [the bottom panel] Bragg peaks.

Mn moments along the NN bond (red bonds) directions in the  $bc$  plane, and such chains are coupled ferromagnetically along the NNN bond (blue bonds) directions in the  $bc$  plane. Therefore, the magnetic structure within the  $bc$  plane is a Néel type AFM. Such antiferromagnetic planes are stacked ferromagnetically along the  $a$  axis (gray bonds). The magnetic structure is purely antiferromagnetic in nature without having any net magnetization per unit cell. The magnetic moments are lying in the  $ac$  plane with moment components  $m_a = 2.60(8)$  and  $m_c = 1.35(28) \mu_B$  per magnetic site ( $\text{Mn}^{2+}$ ) along the  $a$  and  $c$  axes, respectively. The net ordered site moment of Mn ions (considering all the components) is found to be  $M_{\text{total}} = 2.42(3) \mu_B/\text{Mn}^{2+}$  at 1.7 K. The magnetic mo-

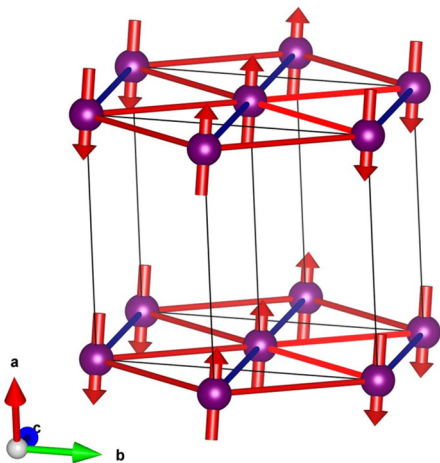


FIG. 8. The magnetic structure of  $\text{Na}_6\text{Mn}(\text{SO}_4)_4$ .

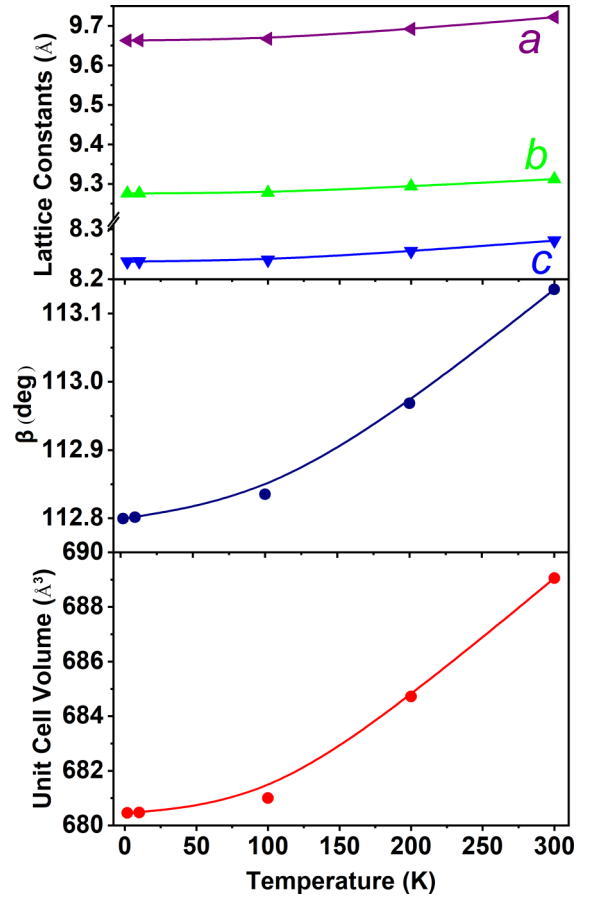


FIG. 9. The temperature-dependent lattice parameters and unit-cell volume of  $\text{Na}_6\text{Mn}(\text{SO}_4)_4$  over the temperature range 1.7–300 K.

ment is found to be strongly reduced from the theoretically expected value of  $4 \mu_B/\text{Mn}^{2+}$  ( $\sim 80\%$  of the fully ordered moment of  $5 \mu_B/\text{Mn}^{2+}$ ), revealing the presence of a strong spin fluctuation at 1.7 K. The temperature variation of the lattice parameters and unit-cell volume is shown in Fig. 9. The change in slope at low temperature could be due to the interaction with magnetic spin and lattice.

### C. Theoretical study of $\text{Na}_6\text{Mn}(\text{SO}_4)_4$

The refined x-ray diffraction data of  $\text{Na}_6\text{Mn}(\text{SO}_4)_4$  (Fig. 1) shows a primitive monoclinic crystal structure in which  $\text{Mn}^{2+}$  ions are placed at each corner of the unit cell and an additional  $\text{Mn}^{2+}$  ion is located at the face-center position in the  $bc$  plane. A careful analysis of the structural information reveals that any  $\text{Mn}^{2+}$  ion located at the corner of the unit cell is connected to four first nearest neighbors along the face diagonal in  $bc$  plane and two second neighbors along the  $c$  axis. This arrangement repeats along the  $a$  axis, as shown in Fig. 10(a). The Heisenberg Hamiltonian is solved on the minimum cluster, which adequately represents the crystal. This involves 14  $\text{Mn}^{2+}$  ions at the vertices and at the center of two hexagons parallel to each other, as shown in Fig. 10(a). The spin of each  $\text{Mn}^{2+}$  ion is  $5/2$  as the crystal field is weak. Exact diagonalization of the 14-site  $s = 5/2$  spin Heisenberg system is computationally prohibitive, as the number of spin orientations (dimensionality of the Fock space) is more than 78 billion. Hence we have replaced the  $s = 5/2$  site spins by

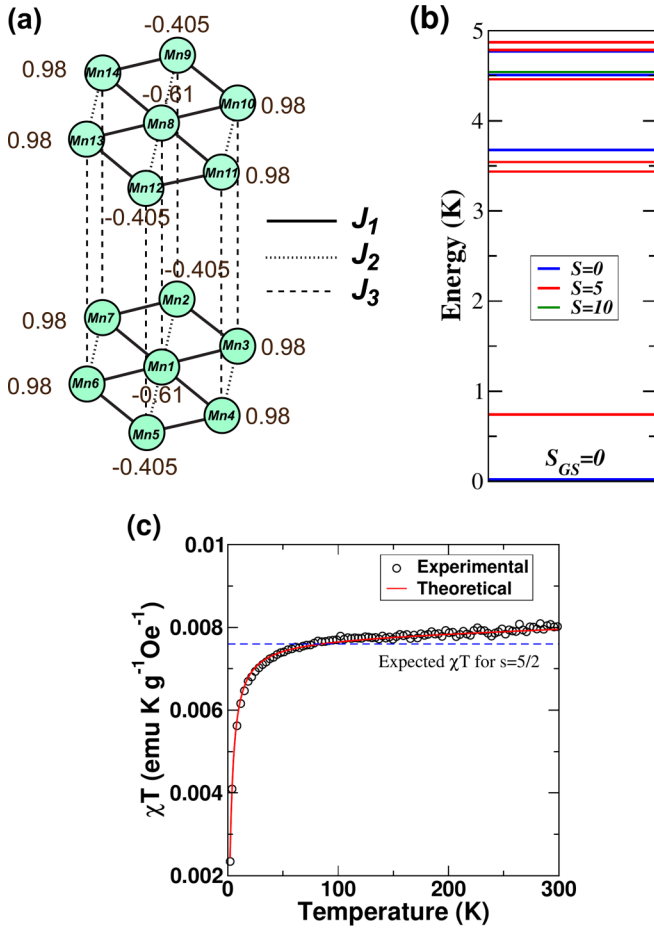


FIG. 10. (a) Schematic of the magnetic exchange interactions in  $\text{Na}_6\text{Mn}(\text{SO}_4)_4$ . The spin densities of the  $S = 5$ ,  $M_S = +5$  state are also shown. The spin density at each Mn site is scaled by a factor of 5 to convert from  $s = 1/2$  to  $s = 5/2$  site spin. (b) Low-lying energy eigenstates of our model in Kelvin along with the total spin of the state. (c) Magnetic susceptibility ( $\chi T$ ) as a function of temperature. Experimental points are shown by circles, and calculated values fall on the red line. Blue line indicates the expected  $\chi T$  value for free  $s = 5/2$  moments.

$s = 1/2$  site spins and have scaled the computed susceptibility by a factor of 11.67, which is the ratio of the square of the magnetic moments of a  $s = 5/2$  ion and  $s = 1/2$  ion. The Fock space dimension of the 14 spin-1/2 system is only 16 384. Furthermore, since the  $z$  component of the total spin,  $S_z$ , is conserved, we can factor the space into different  $M_S$  sectors. Solving the eigensystem for all the eigenvalues and eigenvectors is not computationally intensive and affords exploring the parameter space of the exchange constants in the Hamiltonian on a fine grid.

The magnetic properties are modeled by employing the Heisenberg spin Hamiltonian,

$$\begin{aligned} \hat{H}_0 = & -J_1(\hat{s}_1 \cdot \hat{s}_3 + \hat{s}_1 \cdot \hat{s}_4 + \hat{s}_1 \cdot \hat{s}_6 + \hat{s}_1 \cdot \hat{s}_7 + \hat{s}_2 \cdot \hat{s}_3 \\ & + \hat{s}_4 \cdot \hat{s}_5 + \hat{s}_5 \cdot \hat{s}_6 + \hat{s}_2 \cdot \hat{s}_7 + \hat{s}_8 \cdot \hat{s}_{10} + \hat{s}_8 \cdot \hat{s}_{11} \\ & + \hat{s}_8 \cdot \hat{s}_{13} + \hat{s}_8 \cdot \hat{s}_{14} + \hat{s}_9 \cdot \hat{s}_{10} + \hat{s}_{11} \cdot \hat{s}_{12} + \hat{s}_{12} \cdot \hat{s}_{13} \\ & + \hat{s}_9 \cdot \hat{s}_{14}) - J_2(\hat{s}_1 \cdot \hat{s}_2 + \hat{s}_3 \cdot \hat{s}_4 + \hat{s}_1 \cdot \hat{s}_5 + \hat{s}_6 \cdot \hat{s}_7 \end{aligned}$$

$$\begin{aligned} & + \hat{s}_8 \cdot \hat{s}_9 + \hat{s}_{10} \cdot \hat{s}_{11} + \hat{s}_8 \cdot \hat{s}_{12} + \hat{s}_{13} \cdot \hat{s}_{14}) - J_3(\hat{s}_1 \cdot \hat{s}_8 \\ & + \hat{s}_2 \cdot \hat{s}_9 + \hat{s}_3 \cdot \hat{s}_{10} + \hat{s}_4 \cdot \hat{s}_{11} + \hat{s}_5 \cdot \hat{s}_{12} + \hat{s}_6 \cdot \hat{s}_{13} \\ & + \hat{s}_7 \cdot \hat{s}_{14}), \end{aligned} \quad (2)$$

where  $J_1$ ,  $J_2$ , and  $J_3$  are the strength of exchange interactions between first, second, and third neighbors, respectively, and  $\hat{s}_i$  are the site spin operators, and the numbers in the subscript represent the site index as in Fig. 10(a). A positive or negative value of  $J$  corresponds to a ferromagnetic or antiferromagnetic exchange interaction respectively. The three unique exchange parameters,  $J_1$ ,  $J_2$ , and  $J_3$ , are all antiferromagnetic and have their strengths that are exponentially dependent on the distance between ions; hence  $|J_1| > |J_2| > |J_3|$ . The exchange constants  $J_2$  and  $J_3$  are expressed as fractions of  $J_1$ , which is set to  $-1.0$ . We have taken the two exchange constants,  $J_2$  and  $J_3$ , as  $J_2 = -e^{-r_2/r_1}$  and  $J_3 = -e^{-r_3/r_1}$ , where  $r_1$ ,  $r_2$ , and  $r_3$  are the first, second, and third neighbor distances from the refined x-ray diffraction data. As the first neighbor Mn-O-O-Mn dihedral angle is about  $148^\circ$  (from x-ray structure), we take  $J_1$  to be antiferromagnetic.

The matrix of the spin Hamiltonian [Eq. (2)] was constructed using a basis with constant total  $M_S$ . The largest Hamiltonian matrix, which is  $3432 \times 3432$ , corresponds to the  $M_S = 0$  sector. We obtain the complete eigenspectrum in all the  $M_S$  sectors; this is used to compute the magnetic susceptibility of the system. As the magnetic measurements are carried out under an applied magnetic field, we include a Zeeman term in our calculation, which contributes an energy  $-g\mu_B H_z M_S$  to the eigenstates in a given  $M_S$  sector;  $g$  is the gyromagnetic ratio,  $\mu_B$  is the Bohr magneton, and  $H_z$  is the applied magnetic field. The magnetic susceptibility of the system is given by

$$\chi T = \frac{N_A g^2 \mu_B^2 F(J, T)}{k_B}, \quad (3)$$

$$F(J, T) = \langle M_S^2 \rangle = \frac{\sum_S \sum_{M_S} M_S^2 e^{-\frac{E_0(S, M_S)}{k_B T}}}{\sum_S \sum_{M_S} e^{-\frac{E_0(S, M_S)}{k_B T}}}. \quad (4)$$

In the above expression,  $N_A$  is the Avogadro number,  $k_B$  is the Boltzmann's constant, and  $E_0(S, M_S)$  are energies of the unperturbed Hamiltonian corresponding to the eigenstate with  $z$  component of total spin  $M_S$  [66]. We also add a Curie contribution (C) to the total susceptibility to account for any unreacted residual spin moments left after the synthesis. Besides, our magnetic data shows that the high temperature susceptibility is larger than the  $0.0076 \text{ emu K}/(\text{g Oe})$  expected for free spin-5/2 moments. The  $\chi T$  value also shows a small linear increase with temperature, contrary to the temperature-independent behavior expected in the paramagnetic region for a Curie paramagnet. This suggests that there is an additional temperature-independent susceptibility term or the van Vleck paramagnetic ( $\chi_{VV}$ ) contribution coming from the excited states. The total  $\chi T$  value is given by  $\chi T = \chi T(ex) + \chi T(res) + \chi_{VV} T$ .

The strengths of various exchange interactions are obtained from the parameters that best fit the experimental magnetic data. The experimental magnetic data is fitted in the temperature range 2–300 K [Fig. 10(c)], and best-fit

parameters correspond to  $J_1 = -3.6$  K,  $J_2 = -0.94$  K,  $J_3 = -0.76$  K,  $g = 2.01$ ,  $C = 9 \times 10^{-5}$  emu K / (g Oe), and  $\chi_{VV} = 8 \times 10^{-7}$  emu / (g Oe). The contribution to the susceptibility from Curie-like and temperature-independent paramagnetic concentrations are less than the 3% of the paramagnetic susceptibility of the system obtained by turning off all the exchange interactions. The ground state of the system is a spin singlet ( $S_{GS} = 0$ ) [Fig. 10(b)], confirming an overall antiferromagnetic interaction, as also evidenced from the decreasing  $\chi T$  value as we approach 0 K. The first excited state is an  $S = 5$  state (spin is scaled from  $s = 1/2$  to  $s = 5/2$ ), with an energy gap from the ground state of 0.74 K [Fig. 10(b)]. Besides, there are two more  $S = 5$  states at 3.44 and 3.54 K, before an excited singlet state is found at 3.68 K. Application of magnetic field can significantly lower the energies of states with nonzero magnetization belonging to this  $S = 5$  multiplet. This can lead to trapping of moments in higher magnetization states when the system is cooled under the influence of magnetic field, resulting in the bifurcation of ZFC and FC curves. This is more dominant at low field strengths, as the population of the high spin state is not saturated at these field strengths. Thus, for a small applied field, one observes a substantial change in magnetization on cooling. However, at high field strengths, at about 3 K, the high spin population is almost saturated, and this will lead to smaller change in magnetization as the system is cooled. Hence the ZFC and FC susceptibility curves lie very close to each other. The first excited state with spin  $S = 5$  at 0.74 K has significant thermal population when cooled to 1.7 K, which is the lowest temperature at which the study is carried out. To obtain the magnetic structure of the system, we calculated the spin-spin correlations in the ground state. The spin correlations within the  $bc$  plane agree well with the magnetic structure obtained from neutron diffraction. However, the spin correlations between spins along the  $a$  axis are weak. The

finite-size effects, due to the small system size used in the modeling, do not allow us to definitively conclude the spin alignments along the  $a$  axis. To overcome this difficulty, we calculated spin densities in the lowest excited state, which has total spin  $S = 5$  and which is 0.74 K (which is much lower than the lowest temperature at which the neutron diffraction is carried out) above the singlet ground state. The site spin densities are calculated as expectation values of  $\langle s_i^z \rangle$  in the excited eigenstate with  $S = 5$  and  $M_S = 5$ , corresponding to a fully polarized spin state. The spin densities are shown in Fig. 10(a) and are in agreement with the spin structure obtained from the neutron data shown in Fig. 8.

#### IV. CONCLUSIONS

In summary, the vanthoffite mineral  $\text{Na}_6\text{Mn}(\text{SO}_4)_4$  yields a layered-type crystal structure with distorted triangular lattice arrangements of  $\text{Mn}^{2+}$  ions, and the measurement of magnetic properties shows antiferromagnetic characteristics below 3 K. Neutron diffraction refinements at 1.7 K clearly show an antiferromagnetic spin arrangement in the  $bc$  plane of the structure. Numerical results from the full diagonalization approach also support the experimental results and unambiguously show the presence of antiferromagnetic interactions and singlet magnetic ground state in  $\text{Na}_6\text{Mn}(\text{SO}_4)_4$ . Our neutron diffraction study reveals a collinear antiferromagnetic structure, consistent with the previously proposed ground state of a distorted  $J_1 - J_2$  triangular lattice.

#### ACKNOWLEDGMENTS

T.N.G. and S.R. would like to thank Department of Science and Technology (DST) and INSA for financial support. A.D. would like to thank IISc for funding.

- 
- [1] A. K. Padhi, K. S. Nanjundaswamy, and J. B. Goodenough, *J. Electrochem. Soc.* **144**, 1188 (1997).
- [2] J. Wang and X. Sun, *Energy Environ. Sci.* **8**, 1110 (2015).
- [3] C. Masquelier and L. Croguennec, *Chem. Rev.* **113**, 6552 (2013).
- [4] B. C. Melot and J.-M. Tarascon, *Acc. Chem. Res.* **46**, 1226 (2013).
- [5] Z. Gong and Y. Yang, *Energy Environ. Sci.* **4**, 3223 (2011).
- [6] G. Rousse and J. M. Tarascon, *Chem. Mater.* **26**, 394 (2014).
- [7] M. Reynaud, J. Rodríguez-Carvajal, J.-N. Chotard, J.-M. Tarascon, and G. Rousse, *Phys. Rev. B* **89**, 104419 (2014).
- [8] L. Lander, M. Reynaud, J. Rodríguez-Carvajal, J.-M. Tarascon, and G. Rousse, *Inorg. Chem.* **55**, 11760 (2016).
- [9] R. Toft-Petersen, N.H. Andersen, H. Li, J. Li, W. Tian, S.L. Bud'ko, T.B.S. Jensen, C. Niedermayer, M. Laver, O. Zaharko, J.W. Lynn, and D. Vaknin, *Phys. Rev. B* **85**, 224415 (2012).
- [10] J. Li, W. Tian, Y. Chen, J. L. Zarestky, J. W. Lynn, and D. Vaknin, *Phys. Rev. B* **79**, 144410 (2009).
- [11] T. H. O'Dell, *Electron. Power* **11**, 266 (1965).
- [12] E. Fogh, R. Toft-Petersen, E. Ressouche, C. Niedermayer, S. L. Holm, M. Bartkowiak, O. Prokhnenko, S. Sloth, F. W. Isaksen, D. Vaknin, and N. B. Christensen, *Phys. Rev. B* **96**, 104420 (2017).
- [13] L. Lander, G. Rousse, A. M. Abakumov, M. Sougrati, G. Van Tendeloo, and J.-M. Tarascon, *J. Mater. Chem. A* **3**, 19754 (2015).
- [14] A. Scaramucci, E. Bousquet, M. Fechner, M. Mostovoy, and N. A. Spaldin, *Phys. Rev. Lett.* **109**, 197203 (2012).
- [15] I. Kornev, M. Bichurin, J.-P. Rivera, S. Gentil, H. Schmid, A. G. M. Jansen, and P. Wyder, *Phys. Rev. B* **62**, 12247 (2000).
- [16] M. Fiebig, *J. Phys. D: Appl. Phys.* **38**, R123 (2005).
- [17] B. B. Van Aken, J.-P. Rivera, H. Schmid, and M. Fiebig, *Nature (London)* **449**, 702 (2007).
- [18] E. Bousquet, N. A. Spaldin, and K. T. Delaney, *Phys. Rev. Lett.* **106**, 107202 (2011).
- [19] J.-P. Rivera, *Eur. Phys. J. B* **71**, 299 (2009).
- [20] G. Rousse, J. Rodríguez-Carvajal, C. Wurm, and C. Masquelier, *Phys. Rev. B* **88**, 214433 (2013).
- [21] P. Yanda and A. Sundaresan, in *Advances in the Chemistry and Physics of Materials: Overview of Selected Topics* (World Scientific, Singapore, 2020), p. 224.

- [22] G. T. Rado, J. M. Ferrari, and W. G. Maisch, *Phys. Rev. B* **29**, 4041 (1984).
- [23] S. Bluck and H. G. Kahle, *J. Phys. C: Solid State Phys.* **21**, 5193 (1988).
- [24] M. Reynaud, G. Rousse, J.-N. Chotard, J. Rodríguez-Carvajal, and J.-M. Tarascon, *Inorg. Chem.* **52**, 10456 (2013).
- [25] M. Sun, G. Rousse, A. M. Abakumov, M. Saubanere, M.-L. Doublet, J. Rodríguez-Carvajal, G. Van Tendeloo, and J.-M. Tarascon, *Chem. Mater.* **27**, 3077 (2015).
- [26] G. Rousse, J. Rodríguez-Carvajal, C. Giacobbe, M. Sun, O. Vaccarelli, and G. Radtke, *Phys. Rev. B* **95**, 144103 (2017).
- [27] A. Furrer, A. Podlesnyak, J. M. Clemente-Juan, E. Pomjakushina, and H. U. Güdel, *Phys. Rev. B* **101**, 224417 (2020).
- [28] D. Vagnin, J. L. Zarestky, L. L. Miller, J.-P. Rivera, and H. Schmid, *Phys. Rev. B* **65**, 224414 (2002).
- [29] G. Rousse, J. Rodriguez-Carvajal, S. Patoux, and C. Masquelier, *Chem. Mater.* **15**, 4082 (2003).
- [30] D. Vagnin, J. L. Zarestky, J.-P. Rivera, and H. Schmid, *Phys. Rev. Lett.* **92**, 207201 (2004).
- [31] S. Gnewuch and E. E. Rodriguez, *Inorg. Chem.* **59**, 5883 (2020).
- [32] E. Fogh, O. Zaharko, J. Schefer, C. Niedermayer, S. Holm-Dahlin, M. K. Sørensen, A. B. Kristensen, N. H. Andersen, D. Vagnin, N. B. Christensen, and R. Toft-Petersen, *Phys. Rev. B* **99**, 104421 (2019).
- [33] P. W. Anderson, *Phys. Rev.* **115**, 2 (1959).
- [34] J. Kanamori, *J. Phys. Chem. Solids* **10**, 87 (1959).
- [35] J. B. Goodenough, *Phys. Rev.* **100**, 564 (1955).
- [36] J. B. Goodenough, *J. Phys. Chem. Solids* **6**, 287 (1958).
- [37] J. B. Goodenough, A. Wold, R. J. Arnett, and N. Menyuk, *Phys. Rev.* **124**, 373 (1961).
- [38] G. Rousse, J. Rodriguez-Carvajal, C. Wurm, and C. Masquelier, *Chem. Mater.* **13**, 4527 (2001).
- [39] B. C. Frazer and P. J. Brown, *Phys. Rev.* **125**, 1283 (1962).
- [40] D. Swain and T. N. Guru Row, *Chem. Mater.* **19**, 347 (2007).
- [41] D. Swain and T. N. Guru Row, *Inorg. Chem.* **48**, 7048 (2009).
- [42] G. K. Pradhan, D. Swain, T. N. Guru Row, and C. Narayana, *J. Phys. Chem. A* **113**, 1505 (2009).
- [43] D. Saha, G. Madras, and T. N. Guru Row, *Cryst. Growth Des.* **11**, 3213 (2011).
- [44] V. Sharma, D. Swain, and T. N. Guru Row, *Inorg. Chem.* **56**, 6048 (2017).
- [45] A. Dutta, D. Swain, J. Sunil, C. Narayana, and T. N. Guru Row, *Inorg. Chem.* **59**, 8424 (2020).
- [46] K. L. Keester and W. Eysel, *Acta Crystallogr., Sect. B: Struct. Sci.* **33**, 306 (1977).
- [47] W. M. Zhang, W. M. Saslow, and M. Gabay, *Phys. Rev. B* **44**, 5129 (1991).
- [48] T. Degen, M. Sadki, E. Bron, U. Konig, and G. Nenert, *Powder Diffr.* **29**, S13 (2014).
- [49] V. Petříček, M. Dušek, and L. Palatinus, *Z. Kristallogr.* **229**, 345 (2014).
- [50] V. Siruguri, S. M. Yusuf, and V. C. Rakhecha, *Neutron News* **11**, 4 (2000).
- [51] J. Rodríguez-Carvajal, *Phys. B: Condens. Matter* **192**, 55 (1993).
- [52] A. K. Bera and S. M. Yusuf, *J. Phys. Chem. C* **124**, 4421 (2020).
- [53] A. K. Bera, S. M. Yusuf, S. S. Meena, C. Sow, P. S. A. Kumar, and S. Banerjee, *Mater. Res. Express* **2**, 026102 (2015).
- [54] A. K. Bera, S. M. Yusuf, and S. Banerjee, *Solid State Sci.* **16**, 57 (2013).
- [55] R. Saha, A. Shireen, A. K. Bera, S. N. Shirodkar, Y. Sundarayya, N. Kalarikkal, S. M. Yusuf, U. V. Waghmare, A. Sundaresan, and C. N. R. Rao, *J. Solid State Chem.* **184**, 494 (2011).
- [56] P. B. Moore, *Am. Mineral.* **58**, 32 (1973).
- [57] H. Lu, C. Xiao, R. Song, T. Li, A. E. Maughan, A. Levin, R. Brunecky, J. J. Berry, D. B. Mitzi, V. Blum, and M. C. Beard, *J. Am. Chem. Soc.* **142**, 13030 (2020).
- [58] W. H. Baur, *Acta Crystallogr., Sect. B: Struct. Sci.* **30**, 1195 (1974).
- [59] K. Robinson, G. V. Gibbs, and P. H. Ribbe, *Science* **172**, 567 (1971).
- [60] I. D. Brown and D. Altermatt, *Acta Crystallogr., Sect. B: Struct. Sci.* **41**, 244 (1985).
- [61] A. K. Bera, S. M. Yusuf, L. Keller, F. Yokaichiya, and J. R. Stewart, *Phys. Rev. B* **105**, 014410 (2022).
- [62] P. Suresh, K. Vijaya Laxmi, A. K. Bera, S. M. Yusuf, B. L. Chittari, J. Jung, and P. S. Anil Kumar, *Phys. Rev. B* **97**, 184419 (2018).
- [63] A. K. Bera, S. M. Yusuf, A. Kumar, and C. Ritter, *Phys. Rev. B* **95**, 094424 (2017).
- [64] A. K. Bera, S. M. Yusuf, A. Kumar, M. Majumder, K. Ghoshray, and L. Keller, *Phys. Rev. B* **93**, 184409 (2016).
- [65] J. Rodriguez-Carvajal, FULLPROF suite, [www.ill.eu/sites/fullprof/](http://www.ill.eu/sites/fullprof/).
- [66] O. Kahn, *Molecular Magnetism* (VCH Publishers, Inc., Weinheim, Germany, 1993), p. 393.